JASA EXPRESS LETTERS ARTICLE asa.scitation.org/journal/jel

Scattering measurements of rocky seafloors using a split-beam echosounder

Jen A. Gruber and Derek R. Olson[a)]
Oceanography Department, Naval Postgraduate School, Monterey, California 93943, USA
jenillee.pajewski@gmail.com, derek.olson@nps.edu

Abstract: Scattering measurements were made off the coast of Pacific Grove, CA at 200 kHz, in an exposed fractured granite seafloor. Using inertial sensors and a split-beam transducer, data were processed to obtain a range of grazing angles corresponding to scattering strength, and signal processing techniques were used to extract the relevant portion of each ping. The ensonified angular width from a circular aperture is presented. Scattering strength measurements using different assumptions regarding the grazing angle were compared. The empirical Lommel–Seeliger model provided a good fit to measured data with a parameter of −18.4 dB.

[Editor: David R. Dall'Osto] https://doi.org/10.1121/10.0024755

Received: 25 August 2023 **Accepted:** 19 January 2024 **Published Online:** 6 February 2024

1. Introduction

Acoustic scattering from the seafloor results in energy being dispersed in all directions. The angular and frequency dependence of the scattered acoustic field depends on properties of the seafloor. The scattering cross section per unit area per unit solid angle (a measure of the incoherent average scattered intensity) can be used to remotely sense seafloor properties and predict the performance of acoustic target detection systems (Abraham, 2019). Much of the existing theoretical and experimental work on acoustic scattering from the seafloor has focused on sand and mud seafloors [see Jackson and Richardson (2007), Chap. 12, and references therein]. Rocky seafloors can support much larger values of rough surface height and slope than granular sediments, which may cause large amplitude scattering from localized parts of the seafloor and shadowing from others. This spatial non-uniformity leads to statistically non-stationary scattering measurements.

To date, only a few acoustic scattering measurements from rocky seafloors exist. Early measurements were made by Urick (1954) at 55 kHz and McKinney and Anderson (1964) at 100 kHz. Measurements between 2 and 3.5 kHz were made by Soukup and Gragg (2003) in a limestone area off the coast of South Carolina. Recently, Olson *et al.* (2016) measured backscattering strength of rocky outcrops off the southern coast of Norway at 100 kHz. Scattering statistics of this environment were also reported in Gauss *et al.* (2015) and Olson *et al.* (2019) and were found to have large variance compared to the mean backscattered intensity. Rocky seafloors can have a wide variety of geomorphologies, and it is important to understand the acoustic interaction of these statistically non-stationary interfaces at a variety of frequencies.

The principal contribution of the present work is to report measurements of bottom backscattering in a rocky seafloor at approximately 200 kHz off the western coast of Monterey Peninsula, CA. A form of the ensonified angular width for a circular piston transducer is also presented. Another contribution is to detail a method by which a wide variety of grazing angles corresponding to scattering strength measurements can be obtained using a split-beam echosounder with narrow beam width and a platform with significant rotation (primarily the vehicle roll angle). A method is presented to extract the mainlobe portion of the time series from each ping, which was necessary due to the varying water depth and platform motion. An intermediate step in this process is to estimate the depth of the ensonified patch of seafloor. Since the bathymetry in the region has been measured by the California State University, Monterey Bay Seafloor Mapping Laboratory (CSUMB-SML), comparison of these measurements provides a coarse check on the data processing and is used for one of the grazing angle calculations here.

In Sec. 2, an overview of the environmental conditions of the experimental area is given. In Sec. 3, the method to estimate scattering strength and the corresponding grazing angles using a split-beam transducer is detailed. Section 4 reports the scattering measurements using various types of assumptions regarding the seafloor, and the comparison between the bottom detections measured here, and the CSUMB-SML dataset. Conclusions and suggestions for future work are given in Sec. 5.

[a)]Author to whom correspondence should be addressed.

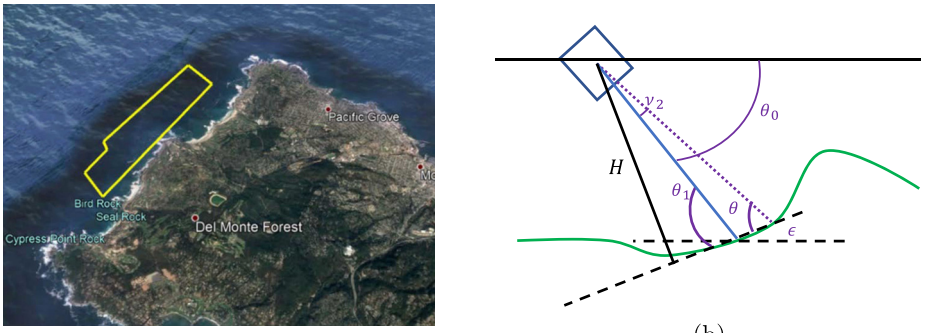

(a) (b)

Fig. 1. (a) Map of Monterey Peninsula with experiment area outlined in yellow. (b) Diagram of various angles used in the scattering measurements.

2. Environment overview

Scattering measurements were conducted off the western coast of Monterey Peninsula, at Asilomar and extending south to Bird Rock, as shown in Fig. 1(a). This experiment area was selected because it contains a rocky seafloor with a very large root mean square (RMS) height. This area was surveyed by the California Geologic Survey (Greene, 1977). It was found to consist of exposed fractured porphyritic granodiorite and had minimal sedimentation, indicating that exposed igneous bedrock was present here. Towed sidescan surveys revealed that in the shallow waters surrounding the peninsula, seafloor roughness is characterized by numerous meter scale outcrops and blocks separated by joints (Eittreim *et al.*, 2002a,b). A diagram of the experiment geometry is shown in Fig. 1(b), indicating the sonar, the relevant angles (explained below) that are used in the processing, and the seafloor.

This area was surveyed by the CSUMB-SML using a multibeam echosounder at a resolution of $2 \times 2\,\mathrm{m}^2$. A three-dimensional (3D) rendering of the bathymetry in the experiment area is shown in Fig. 2(a), with the ship track superimposed at -0.48 m depth (the average tide for the measurement time and location) and points representing the estimated bathymetry from the echosounder (details of this process are discussed below). For this figure, universal transverse mercator (UTM) coordinates were rotated 30° counterclockwise, so that the two horizontal ordinates align with the along-shore and across-shore directions. A plane was fit to this bathymetry of the form $z = ax + by + c$ using least squares, where x is the along-shore direction, y is the cross-shore direction, z is the ocean depth, and $(a, b, c) = (0.01, 10^{-4}, 5\,\mathrm{m})$ are constants. After this plane was subtracted from the bathymetry, it had an RMS

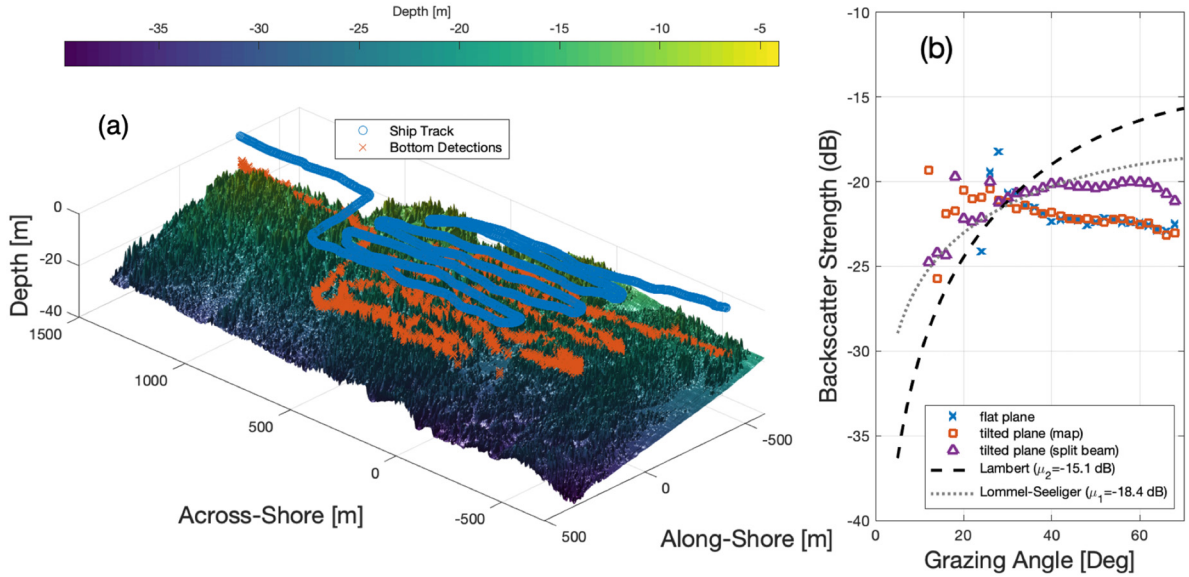

Fig. 2. (a) Comparison of estimated bathymetry with ground truth from CSUMB plotted in across-shore and along-shore coordinates. Both the ship track and bottom detections are plotted. (b) Scattering strength versus grazing angle results for the three different methods and two model fits to the split-beam results.

value of approximately 2.2 m and an RMS slope of 60°. This is considered to be a very rough seafloor for the high frequency system used here (with a wavelength of 7.5 mm). The scattered field is likely also influenced by biological organisms, especially shellfish, and kelp root systems (which produce bubbles) that are often present on these rock surfaces.

3. Experiment and data processing

Measurements were performed using a 200 kHz split-beam echosounder manufactured by Biosonics Inc. The sonar system was mounted on a pole attached to an 8 m rigid hull inflatable boat (RHIB), and measurements took place on August 2, 2019, between 08:30 and 13:30 local time. From a buoy maintained by Stanford Hopkins Marine Station and part of the National Data Buoy Center [Buoy number 46240 (NDBC, 2023)], the RMS surface wave height was approximately 0.85 m, and swell period varied between 5 and 8 s. The platform followed a lawnmower pattern that is plotted in Fig. 2(a).

3.1 Scattering strength

Scattering strength was estimated using the sonar equation, which relates the received scattered intensity at each sample in time to a single angle and the scattering strength at that angle. The sonar equation used here is [Jackson and Richardson (2007), Appendix G]

$$\langle |v|^2 \rangle = s^2 \frac{e^{-4k_w'' r_t}}{r_t^4} D_{TX} D_{RX} \sigma \left(\frac{c_w \tau}{2} r_t \Psi_t \right). \tag{1}$$

The left-hand side is the mean square digitized voltage output by the receiver electronics. The source/receiver parameter, s, with units of V × m is the product of the pressure version of the source level (units of μPa × m) and receiver sensitivity (units of V/μPa). These parameters were measured independently using reference transducers and cables by the sonar manufacturer, and their product is $s = 1.58 \times 10^{17}$ V × m. The measurement error of transducer properties was reported by the manufacturer to be ±0.1 dB. The calibration was performed just prior to delivery of the system in 2019 and is a relatively good characterization of the state of the system during the experiment.

Attenuation is parameterized using the imaginary part of the wavenumber in water, k_w''. The real part of the wavenumber in water is $k_w = 2\pi f / c_w$, where f is the acoustic frequency, and c_w is the adiabatic speed of sound in water. Both of these are assumed to be constant and are calculated using temperature from Buoy 46240 (NDBC, 2023), climatological values of salinity, and a depth of 10 m. The range between the ensonified patch of seafloor and the sonar is $r_t = c_w t/2$, where t is the time since the pulse was transmitted. The duration of the transmitted rectangular pulse is $\tau = 0.1$ ms. The variables D_{TX} and D_{RX} are the vertical transmit and receiver directivity pattern of the transducer evaluated at the ray connecting the source to the resolved patch of seafloor. The beam pattern of this piston transducer was also measured by the manufacturer and has a half-power full width of 6.7° (for both the transmitter and receiver modes). Its shape is well approximated by a Gaussian function with azimuthal symmetry (sidelobe levels are more than 35 dB down from the peak).

The equivalent ensonified angular width at each time sample is Ψ_t, and it depends on the two-way beam pattern of the transducer projected onto the seafloor, integrated over the azimuthal direction. Note that in Appendix G of Jackson and Richardson (2007), a form of Ψ_t is given for rectangular transducers. Here, we give a form of Ψ_t for circular piston transducers with azimuthal symmetry, which to our knowledge is absent in the literature. Ψ_t is calculated using the formula,

$$\Psi_t = \int_{-\pi}^{\pi} b^2(\delta(\phi, \theta, \theta_1)) d\phi, \tag{2}$$

where ϕ is the azimuthal coordinate in the local plane of the seafloor, and δ is the angle from the maximum response axis (MRA) of the transducer (used as the argument of the beam pattern). The grazing angle between the beam axis at each point and the seafloor slope is θ, which is a function of time, and the grazing angle between the MRA and the seafloor slope is θ_1, which we refer to as the nominal grazing angle. For a flat seafloor, θ_1 corresponds with the depression angle of the transducer, χ. These angles are illustrated in Fig. 1(b). The transformation between the azimuthal coordinate in the local seafloor plane, grazing angle, θ, and θ_1 is the function $\delta = \cos^{-1}(\cos(\theta)\cos(\theta_1)\cos(\phi) + \sin(\theta)\sin(\theta_1))$. This formula can be derived by taking the inverse cosine of the dot product between the transducer MRA normal vector and the normal vector pointing to an integration point on the seafloor.

Jackson's method produces a closed form approximation for Ψ_t, in which the factor $1/\cos(\theta)$ is manifest (which takes into account the projection of the sonar pulse onto the plane of the seafloor). However, the beam pattern of this transducer is not horizontally separable, and no analytical result is available. Therefore, the integral is computed using numerical quadrature for each sample in each ping. First, a set of 128 points (chosen so that the integral resulted in less than 1% relative error) and weights is generated using Gauss–Legendre quadrature. The points are transformed from the interval $[-1, 1]$ to $[-\pi, \pi]$, and the weights are multiplied by π to take this transformation into account, resulting in transformed points and weights, ϕ_q and w_q, respectively. These points are transformed from seafloor polar coordinates, (R, ϕ),

onto the angle away from the main response axis, $\delta_q = \delta(\phi_q, \theta, \theta_1)$. The integral can be computed as $\Psi_t = \sum_{q=1}^{128} b^2(\delta_q) w_q$. The one-way beam pattern Gaussian approximation is $b(\delta) = \exp\left(-\delta^2/(b_w/(2\sqrt{\log 2}))^2\right)$, where b_w is the one-way full-width beam width in radians and is 0.1169 radians (6.7°) for this transducer. In this method, the projection factor $1/\cos(\theta)$ is not explicit, but it is correctly taken into account in the integral.

Equation (1) is inverted for an unaveraged version of σ for each ping and then grouped in bin widths of 2° (chosen to balance angular resolution and ensemble size) and averaged. Each sample of each ping has a different value of θ, and each ping has a separate value of θ_1 assigned to it and has a different value of Ψ_t calculated for the inversion. Methods of estimating these two quantities are detailed in Sec. 3.3.

3.2 Estimating relevant portion of each ping

Since the transducer has a 6.7° beam width and has a depression angle of about 50° below horizontal, not all of the time series of each ping is due to interaction with the seafloor. The bathymetry varies significantly in the survey area (between 5 and 30 m), and thus, the relevant portion of each ping will be different. The raw echogram (in dB re V) is shown in Fig. 3(a). The peak echo level (EL) occurs at larger ranges for earlier pings, then moves to shorter ranges near the middle, and then gradually moves to larger ranges for later pings. This trend is due to the varying seafloor depth along the ship's track, which varied between about 5 and 20 m. Small-scale oscillations in the location of peak intensity are evident and are due to platform motion. In the echogram, some other local peaks are visible, making it difficult to select the portion of the data from which scattering strength should be estimated. Early peaks are likely due to side-lobes and scatterers in the water column (such as kelp or fish), and later peaks are likely due to multipath arrivals and side-lobes.

A method was developed to reject ambient noise (appearing both before and after the main return), multipath arrivals (appearing after the main return), and water-column scatterers (appearing before the main seafloor return). First, the EL (in dB re V) is thresholded at T_1 dB re V. Then $30\log_{10}(r_t/r_0)$, where $r_0 = 1$ m is a reference range, is added to the thresholded EL to remove most of the transmission loss and a simple form of the ensonified area. The transformed data are then thresholded at a level of T_2 dB re $(\mathrm{V} \times \mathrm{m}^{3/2})$. Thresholding the raw data at T_1 is effective for removing additive noise, and multipath returns, whereas thresholding the transformed data at T_2 is effective for removing water-column scatterers, since the transformation applies a lower weight to early portions of the time series. The values were chosen by trial and error and visual examination of the thresholded time series for secondary peaks so that as much of the main returns was preserved as possible, but with a larger emphasis on rejecting non-seafloor returns. The thresholds were set at 75 dB re V and 150 dB re $\mathrm{V} \times \mathrm{m}^{3/2}$ for T_1 and T_2, respectively.

Once the data were thresholded, the centroid range, $r_c = \Sigma_{i=1}^{N_r}(r_i v_i^2)/\Sigma_{i=1}^{N_r} v_i^2$, for each ping was estimated, where N_r is the number of points per ping retained after thresholding, i indexes the retained points, r_i is the range, and v_i^2 is the squared voltage. This formula was used under the assumption that this quantity approximately corresponded to the location of the MRA intersecting with the seafloor. It now remains to select the beginning and end sample of the time series. The centroid range and transducer orientation are used to define the intersection point of the ensonified pulse of the seafloor, $\mathbf{r}_{int}$. This is accomplished by converting the transducer coordinate system into the Earth coordinate system, through

$$\mathbf{r}_{int} = \mathbf{R}(\alpha, \beta, \gamma)(r_c, 0, 0)^T, \tag{3}$$

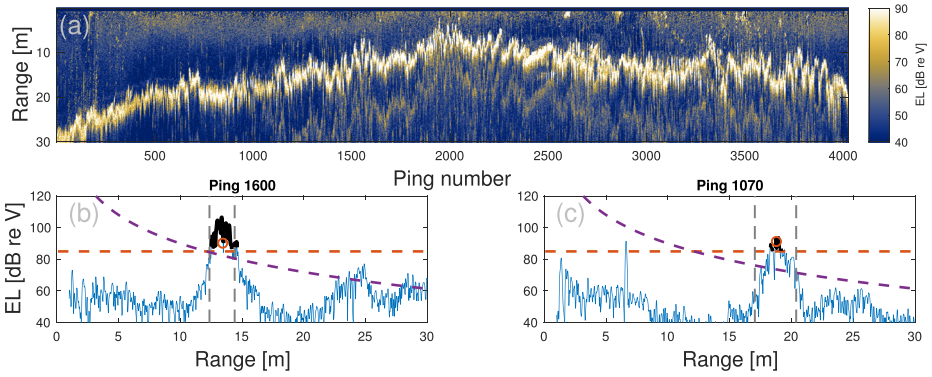

Fig. 3. Example of the data selection process. In (a) the echogram is shown in dB re V as a function of range and ping number. Data from ping 1600 are shown in (b), which has significant multipath at longer ranges, and data from ping 1070 are shown in (c), which has a large water-column scatterer. In both (b) and (c), the thresholds, T_1 and T_2, are shown as red and purple dashed lines, respectively. The centroid is shown as a circle, and the thick line denotes the data used to estimate the centroid. Vertical lines denote the region of data retained for scattering strength estimation.

where $\mathbf{R}(\alpha, \beta, \gamma)$ is the rotation matrix with arguments of roll, pitch, and heading, respectively, that are provided by the orientation sensor within the transducer, and T denotes transposition. The heading angle is corrected for the magnetic declination of the region, 13.01°. This rotation matrix converts from a unit vector pointing due north to the normal vector of the transducer face at a given ping, expressed in a north, east, down (NED) coordinate system. When the vector $(r_c, 0, 0)^T$ is multiplied by the matrix, the resulting vector is the position of the intersection between the MRA and the seafloor in coordinates relative to the boat. The vector of the intersection is used to calculate a nominal depression angle of the sonar, θ_0. Based on a flat seafloor assumption, the effective altitude of the sonar system is $H_{flat} = r_c/\sin(\theta_0)$. We specify upper and lower limits of the time series based on the nominal grazing angle assuming a flat seafloor, $\theta \in [\theta_0 - 1.5b_w, \theta_0 + 1.5b_w]$. These limits are then transformed back into the range domain using $r = H\sin(\theta_0 \pm 1.5b_w)$ and then converted to sample number per ping. Note that this specific flat seafloor assumption is only used to determine the beginning and end of each ping, not to compute the values of the nominal grazing angle θ_1.

An illustration of this process is shown in Fig. 3. The entire echogram is shown in Fig. 3(a) as the EL in dB re V. The broad peaks correspond to the main seafloor return. This location changes throughout the experiment as the water depth changes. Small variations are due to changes in the elevation angle of the sonar due to platform rotation. Ping 1600 in Fig. 3(b) shows significant multipath returns at later times, and ping 1070, shown in Fig. 3(c), has a strong water-column scatterer. Figures 3(b) and 3(c) also show the thresholding processes, the centroid location, data retained for centroid estimation, and the limits of retained data (with the lines corresponding to these quantities explained in the figure caption).

3.3 Estimating grazing angle and nominal grazing angle

Three different methods are used here to estimate the grazing angle, θ, to which the scattering cross section measurements correspond. The angles used below are shown graphically in Fig. 1(b), and several were described in Sec. 3.1. Note that θ_0, the nominal depression angle, is determined both by the sonar mounting angle on the platform and its attitude during a given ping (primarily roll and pitch). The angle ϵ is the seafloor slope angle along the direction of the sonar beam, and H is the effective altitude in the plane of the ensonified patch.

The first method uses the assumption that the seafloor is a perfect horizontal plane (with a different depth for each ping). The vector pointing from the transducer to the per-sample ensonified point on the seafloor, $\mathbf{r}_{flat}(t)$, is calculated using Eq. (3) with $r(t) = c_w t/2$ in place of r_c. The unit vector of $\mathbf{r}_{flat}$ is $\hat{\mathbf{r}}_{flat} = \mathbf{r}_{flat}/|\mathbf{r}_{flat}|$. The normal vector of the assumed flat seafloor is $\hat{\mathbf{n}}_{flat} = (0, 0, -1)^T$. The nominal grazing angle is calculated using $\theta_1 = \pi/2 - \cos^{-1}(\hat{\mathbf{r}}_{int} \cdot \hat{\mathbf{n}}_{flat})$. The effective altitude of the sonar over this flat seafloor is $H_{flat} = \mathbf{r}_{flat} \cdot \hat{\mathbf{n}}_{flat}$, and the grazing angle per sample is $\theta(t) = \sin^{-1}(H_{flat}/r(t))$.

The second method of estimating grazing angle uses the CSUMB-SML bathymetry to calculate the local seafloor normal vector and, thus, takes into account seafloor features that are larger than the 2 m grid resolution. The seafloor intersection vector is the same as for the first method, $\mathbf{r}_{flat}$. The position of intersection with the seafloor is $(\mathbf{r}_{flat} \cdot \hat{x} + x_0, \mathbf{r}_{flat} \cdot \hat{y} + y_0, \mathbf{r}_{flat} \cdot \hat{z} + z_0)^T$. The northing and easting positions (x_0 and y_0, respectively) were found using the GPS receiver in the sonar processor, and z_0 is the negative of the tide level at the time of the given ping reported by Buoy 46240 (NDBC, 2023). A set of points from the map in a 5 m radius around the point of intersection of the MRA and the seafloor is found for each ping. Coefficients of the equation $a_b x + b_b y + c_b z + d_b = 0$ were fit to these points using least squares. The plane fit accounts for "tilt" along the MRA of the sonar, as well as the "tip" across this direction. The normal vector of this plane is $\hat{\mathbf{n}}_{bathy} = (a_b, b_b, c_b)^T/\sqrt{a_b^2 + b_b^2 + c_b^2}$. The angle θ_1 is calculated using $\theta_1 = \pi/2 - \cos^{-1}(\hat{\mathbf{r}}_{flat} \cdot \hat{\mathbf{n}}_{bathy})$. The effective altitude is the point of closest approach between the sonar location and the plane fit to the bathymetry, $H_{bt} = (a_b x_0 + b_b y_0)^T/\sqrt{a_b^2 + b_b^2 + c_b^2}$. The per-sample grazing angle in this case is calculated using the time-dependent range and effective altitude $\theta(t) = \sin^{-1}(H_{bt}/r(t))$.

The third method uses the split-beam sensors of the sonar to estimate local bathymetry of the ensonified region. There are two split-beam channels, ν_1 and ν_2. If the transducer face normal points horizontally in the north direction with the connector port pointing up, then the ν_1 denotes the angle in the east-west direction, and ν_2 denotes angles in the up-down direction. In this case, positive angles correspond to east and down, respectively. The position corresponding to the two-way travel time, t, measured by the split-beam system relative to the ship is

$$\mathbf{r}_{sb} = R(\alpha, \beta, \gamma)(r(t)\cos(\nu_1), r_d, r(t)\cos(\nu_2))^T, \tag{4}$$

where $r_d = r(t)\sqrt{1 - \cos^2(\nu_1) - \cos^2(\nu_2)}$. This position results in a set of points, $\mathbf{r}_{sb} = (x_{sb}, y_{sb}, z_{sb})^T$. Due the random nature of seafloor scattering and the presence of noise, there is some uncertainty in the ν_1 and ν_2 channels and, therefore, some uncertainty the set of seafloor points. We address this noise by forming a planar fit, using $a_{sb}x_{sb} + b_{sb}y_{sb} + c_{sb}z_{sb} + d_{sb} = 0$. The normal vector of this plane is $\hat{\mathbf{n}}_{sb} = (a_{sb}, b_{sb}, c_{sb})^T/\sqrt{a_{sb}^2 + b_{sb}^2 + c_{sb}^2}$. The values for θ_1, effective altitude for this plane, and the per-sample grazing angle are calculated using the sonar range, and the plane coefficients are calculated in a similar fashion as the bathymetry-derived grazing angle (discussed above), but with coefficients derived from $\mathbf{r}_{sb}$ and $\hat{\mathbf{n}}_{sb}$.

4. Results and discussion

The two major results of this paper are (1) the estimated bottom detection points compared with the ground truth and (2) the scattering strength using three different assumptions regarding the bottom slope and position. A comparison of the ground-truth CSUMB-SML bathymetry and the bottom detections is shown in Fig. 2(a). The bathymetry is shown as the colormap, the ship track positions as blue circles, and bottom detections as red exes. The bottom detections generally follow the ground truth bathymetry but have small deviations. One source of deviations is due to surface gravity waves, since the GPS receiver does not report altitude. Additionally, bathymetric features too small to be resolved by the CSUMB-SML dataset but observable using this system could be responsible. Spurious detections in the water column may also play a role, but the effect of these is small due to the thresholding process described earlier.

Scattering strength using each method of determining θ, θ_1, and Ψ_t is shown in Fig. 2(b). Both the flat seafloor and bathymetric plane methods give very similar results. This is likely because the cross-shore seafloor slope is the dominant effect in the approximately 80 m^2 patch that is used to estimate the plane coefficients. This slope is less than the 2° bin width and, therefore, is unlikely to cause deviation from the flat interface assumption. The split-beam scattering strength is generally higher by 1–2 dB at high-to-moderate grazing angles, which is due to the dependence of the Ψ_t term in the sonar equation on θ_1 and θ. Another notable difference is that the flat and map-based scattering strengths increase slightly as θ decreases (between 20° and 70° grazing angle), whereas the split-beam version of scattering strength either remains approximately constant or decreases with decreasing grazing angle (apart from minor fluctuations). In examining other measurements of scattering strength from very rough rock surfaces at moderate grazing angles (cited in Sec. 1), scattering strength is typically either flat or decreases as grazing angle decreases, which agrees more with measurements using the split-beam angles. It is possible that for this very rough rock surface with RMS slope of approximately 60°, measuring the angles near the scale of the ensonified area is necessary for an accurate measurement. Note that the measurements by Olson *et al.* (2016) also used acoustically derived seafloor slopes of rock outcrops off the coast of Norway. Although water-column scatterers were specifically rejected by our thresholding approach, it is possible that a small percentage of the data was contaminated by water-column scatterers that are very close to the main return. This would bias the scattering strength toward higher scattering strength, but since the overall fraction of isolated scatterers that pass the thresholding process is minuscule, the overall effect is likely to be negligible.

Two empirical models are fit to the split-beam data, $\sigma_1 = \mu_1 \sin\theta$, which is the Lommel–Seeliger model (Fairbairn, 1999), and $\sigma_2 = \mu_2 \sin^2\theta$, which is Lambert's model (Jackson and Richardson, 2007). Lambert's model is typically used to model scattering from very rough surfaces and provided a good fit to measurements of scattering from rock seafloors at 100 kHz (Jackson and Richardson, 2007; Olson *et al.*, 2016). Lommel–Seeliger models volume scatterers distributed in an attenuating layer beneath an interface (Fairbairn, 1999). Overall, the scattering strength is nearly flat for all three measurements between about 20° and 70° grazing angle. This angle independence indicates that the scattered field is highly diffuse, perhaps more so than both empirical models used here. Similar flat behavior of scattering strength was seen in numerical simulations of rough scattering from faceted surfaces in Olson (2014). It is possible that diffraction from corners in the rock outcrop (or from shellfish living on them) causes the highly diffuse scattered field at moderate grazing angles.

The data appear to follow Lambert's law more at small angles and the Lommel–Seeliger model at moderate angles. The Lommel–Seeliger model environment is similar to a layer of biological organisms overlying the rocky basement. What would be measured is the effective interface scattering cross section of the rock-kelp system, rather than the scattering cross section of bare rock. It is possible that scattering from biological organisms is more dominant at steeper angles, whereas diffuse scattering from the rock surface is dominant at shallower angles. Further physics based modeling and detailed ground-truth measurements are needed to evaluate these hypotheses.

At an angle of 30°, scattering strength is approximately −20 dB for these measurements. Previous measurements at 30° from rocky environments resulted in scattering strengths of −21 dB (Olson *et al.*, 2016) at 100 kHz, −19 dB at 3.5 kHz (Soukup and Gragg, 2003), −21 dB at 100 kHz (McKinney and Anderson, 1964), and −13 dB at 55 kHz (Urick, 1954). Apart from the Urick results, scattering strength measured in this work is within a few decibels of other work at frequencies of 100 kHz or more. Given that many of these measurements have unknown geomorphology and were made at a variety of different frequencies, it is difficult to draw firm conclusions from this comparison.

Differing behavior of the scattering strengths resulting from the various angle estimation methods motivates examination of the differences between the bathymetry and seafloor slope measured by each method. Figure 4(a) presents the per ping bathymetry difference between the split-beam measurements and the ground truth, with Fig. 4(b) containing the probability density function (PDF) of this variable. Overall, the bathymetric measurements are accurate, with a 0.9 m mean of the PDF. This offset is quite close to the depth below the waterline at which the transducer was mounted. The standard deviation of this PDF is approximately 1.1 m, which is similar to the RMS wave height of 0.85 m. Therefore, the bottom detections obtained are reasonable given the sources of error, which indicates that the method described here to extract the relevant portion of the time series of each ping is sound. The bathymetry differences appear to be uncorrelated with neighboring pings, and there is no systematic trend in along-shore and across-shore position.

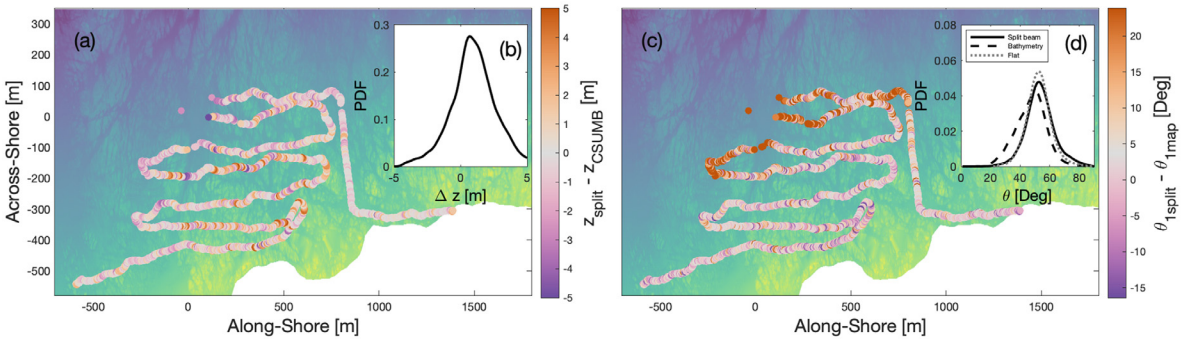

Fig. 4. (a) Difference between the estimated and ground-truth bathymetry (dot in the orange purple colormap) overlaid on the CSUMB ground-truth bathymetry [same colormap as Fig. 3(a)]. (b) Difference between the seafloor slope calculated using the acoustic measurements and using the CSUMB ground truth. (c) PDF of the bathymetry difference. (d) PDF of the slope difference.

In Fig. 4(c), the per ping seafloor slope difference along the direction of the sonar beam is plotted. This quantity is expressed in terms of the slope angle in degrees. For most of the dataset, the differences appear to be uncorrelated with neighboring pings, but for some of the samples in the upper left-hand portion of the plot (the southeastern edge of the experiment area), the differences are large, about 20°, and steady for a large portion of pings. These differences may be due to some bathymetric features that are not present in the CSUMB dataset (which is possible, since the authors have observed a small amount of sediment transport in this area, and boulders are occasionally dislodged by wave action) or may be an artifact of low signal-to-noise ratio (SNR) in these areas (at larger ranges). These differences underscore the potential for error introduced in the split-beam angle measurement. In Fig. 4(d), the PDF of θ, the grazing angle per ping per sample, for the three different angle measurement techniques is shown. The flat seafloor assumption has a very similar PDF as the split-beam measurements, but has slightly more high angle samples. The map-based method has more low-angle samples. The angles measured by all three methods are between 0° and 90° and do not show non-physical behavior.

5. Conclusion

Measurements of the bottom scattering strength in a rocky seafloor have been detailed. The significant platform attitude variation allowed a larger range of grazing angles to be interrogated than would otherwise be possible using a narrow-beam sonar system. The results shown here agree to within several dB with previous very high frequency (i.e., at or above 100 kHz) measurements of bottom scattering in rocky areas. The mechanisms responsible for scattering in this area are varied, including interface scattering from very rough surfaces, tilting of facets (Lyons *et al.*, 2022; McDaniel and Gorman, 1983; Olson and Lyons, 2021), shadowing (Wagner, 1967), multiple scattering (Ishimaru and Chen, 1990; Liszka and McCoy, 1982), and scattering and absorption from biological organisms that are abundant in this area. An interesting area for future work is on theoretical models for scattering strength of this very complex environment.

Acknowledgments

The authors thank Keith Wyckoff of the Naval Postgraduate School for operating the research vessel, providing logistical support, and fabricating the sonar mount. Funding was provided by the Office of Naval Research and the Naval Postgraduate School Undersea Warfare Program. Bathymetry data were provided by the Seafloor Mapping Laboratory at California State University, Monterey Bay.

Author Declarations

Conflict of Interest

The authors have no conflicts of interest to declare.

Data Availability

The data that support the findings of this study are available from the corresponding author upon reasonable request.

References

Abraham, D. A. (**2019**). *Underwater Acoustic Signal Processing* (Springer, Cham, Switzerland).

Eittreim, S. L., Anima, R. J., and Stevenson, A. J. (**2002a**). "Erratum to 'Seafloor geology of the Monterey Bay area continental shelf' [Marine Geology 181 (2002) 3–34]," Mar. Geol. **186**(3–4), 583.

Eittreim, S. L., Anima, R. J., and Stevenson, A. J. (**2002b**). "Seafloor geology of the Monterey Bay area continental shelf," Mar. Geol. **181**(1–3), 3–34.

Fairbairn, M. B. (**1999**). "Planetary photometry: The Lommel–Seeliger law," J. R. Astron. Soc. Can. **99**(3), 92–93.

Gauss, R. C., Fialkowski, J. M., Calvo, D. C., Menis, R., Olson, D. R., and Lyons, A. P. (**2015**). "Moment-based method to statistically categorize rock outcrops based on their topographical features," in *Proceedings of OCEANS 2015—MTS/IEEE Washington*, October 19–22, Washington, DC (IEEE, New York).
Greene, H. G. (**1977**). Geology of the Monterey Bay Region, California (U.S. Geological Survey, Denver, CO).
Ishimaru, A., and Chen, J. S. (**1990**). "Scattering from very rough surfaces based on the modified second-order Kirchhoff approximation with angular and propagation shadowing," J. Acoust. Soc. Am. **88**, 1877–1883.
Jackson, D. R., and Richardson, M. D. (**2007**). *High-Frequency Seafloor Acoustics* (Springer, New York).
Liszka, E. G., and McCoy, J. J. (**1982**). "Scattering at a rough boundary—Extensions of the Kirchhoff approximation," J. Acoust. Soc. Am. **71**, 1093–1100.
Lyons, A. P., Olson, D. R., and Hansen, R. E. (**2022**). "Modeling the effect of random roughness on synthetic aperture sonar image statistics," J. Acoust. Soc. Am. **152**(3), 1363–1374.
McDaniel, S. T., and Gorman, A. D. (**1983**). "An examination of the composite-roughness scattering model," J. Acoust. Soc. Am. **73**, 1476–1486.
McKinney, C. M., and Anderson, C. D. (**1964**). "Measurements of backscattering of sound from the ocean bottom," J. Acoust. Soc. Am. **36**, 158–163.
NDBC (**2023**). https://www.ndbc.noaa.gov/download_data.php?filename=46240h2019.txt.gz&dir=data/historical/stdmet/ (Last viewed August 23, 2023).
Olson, D. R. (**2014**). "High-frequency acoustic scattering from rough elastic surfaces," Ph.D. thesis, The Pennsylvania State University, State College, PA.
Olson, D. R., and Lyons, A. P. (**2021**). "Resolution dependence of rough surface scattering using a power law roughness spectrum," J. Acoust. Soc. Am. **149**(1), 28–48.
Olson, D. R., Lyons, A. P., Abraham, D. A., and Saebø, T. O. (**2019**). "Scattering statistics of rock outcrops: Model-data comparisons and Bayesian inference using mixture distributions," J. Acoust. Soc. Am. **145**(2), 761–774.
Olson, D. R., Lyons, A. P., and Saebø, T. O. (**2016**). "Measurements of high-frequency acoustic scattering from glacially eroded rock outcrops," J. Acoust. Soc. Am. **139**(4), 1833–1847.
Soukup, R. J., and Gragg, R. F. (**2003**). "Backscatter from a limestone seafloor at 2–3.4 kHz: Measurements and modeling," J. Acoust. Soc. Am. **113**, 2501–2514.
Urick, R. J. (**1954**). "The backscattering of sound from a harbor bottom," J. Acoust. Soc. Am. **26**, 231–235.
Wagner, R. J. (**1967**). "Shadowing of randomly rough surfaces," J. Acoust. Soc. Am. **41**, 138–147.